Linear colossal magnetoresistance and magnetic textures in LaTiO₃ thin films on SrTiO₃

Teresa Tschirner [1,2], Berengar Leikert [2,3], Felix Kern,[1] Daniel Wolf,[1] Axel Lubk,[1,2,4] Martin Kamp [2,3],
Kirill Miller,[2,3] Fabian Hartmann,[2,3] Sven Höfling [2,3], Judith Gabel,[5] Matthias Schmitt [5], Martin Stübinger,[2,3]
Julia Küspert [2,3], Tien-Lin Lee,[5] Bernd Büchner,[1,2,4] Joseph Dufouleur [1,2], Marc Gabay,[6] Michael Sing,[2,3]
Ralph Claessen [2,3], and Louis Veyrat [1,2,3]

[1]*Leibniz Institute for Solid State and Materials Research, IFW Dresden, Helmholtzstrasse 20, 01069 Dresden, Germany*
[2]*Würzburg-Dresden Cluster of Excellence ct.qmat, 97074 Würzburg, Germany*
[3]*Physikalisches Institut, Universität Würzburg, D-97074 Würzburg, Germany*
[4]*Institute of Solid State and Materials Physics, TU Dresden, 01069 Dresden, Germany*
[5]*Diamond Light Source, Harwell Science and Innovation Campus, Didcot OX11 0DE, United Kingdom*
[6]*Laboratoire de Physique des Solides, Université Paris-Saclay, CNRS UMR 8502, 91405 Orsay, France*

Linear magnetoresistance (LMR) is of particular interest for memory, electronics, and sensing applications, especially when it does not saturate over a wide range of magnetic fields. Structural disorder, however, also tends to limit the mobility and hence the overall LMR amplitude. An alternative route to achieve large LMR is via nonstructural inhomogeneities which do not affect the zero field mobility, like magnetic domains. Here, we report a colossal positive linear magnetoresistance in LaTiO₃/SrTiO₃ heterostructures, with amplitude up to 6500% at 9T at low temperature. The colossal amplitude of the LMR, one of the largest in oxide heterostructure, stems from the unusual combination of a very high heterostructure mobility, up to 40 000 cm² V⁻¹ s⁻¹, and a very large coverage of low-mobility regions. Low-temperature Lorentz transmission electron microscopy measurements further reveals a striped magnetic structure at the sub-μm scale in the LaTiO₃ layer, compatible with in-plane spiral magnetism, with very high surface coverage. We propose that the low-mobility regions and striped magnetic regions are correlated, we model the increase in scattering induced by the magnetic texture, and we show that the non saturating LMR fits the Parish-Littlewood scenario. Our results provide a novel route for the engineering of large-LMR systems, using magnetic texture.

I. INTRODUCTION

In conventional metals, the magnetoresistance (MR) commonly exhibits quadratic field dependence at low magnetic fields and saturates at high fields [1]. This classical MR is usually limited in amplitude to a few percent at 10T [2]. Many effects, however, are known to impact magnetoresistance: a magnetic ground state (ferromagnetism (FM) [3–8], antiferromagnetism (AFM) [9,10]), Dirac physics [11–13], Landau levels [14,15], or spatial inhomogeneities [16–21], for instance, can lead to modifications of the amplitude or the magnetic field dependency of the MR. In particular, Dirac physics in topological insulators [11–13] and semimetals [22–30] or spatial inhomogeneities [18–20,31] can result in linear magnetoresistance (LMR) behavior [1,16,17,32]. Beyond its relevance for fundamental research, the nonsaturating nature of LMR makes it also interesting for linear magnetoresistance sensors with high resolution, and potential memory reading applications [33–35]. In this context, systems with large LMR are highly desirable.

Among other theories, nonsaturating LMR can be understood semiclassically in the Parish-Littlewood framework by a random resistor network model that mimics a disordered and strongly inhomogeneous conductor system [16,17]. This model can be extended to systems with local low-mobility or low-carrier density regions acting as guiding centres for the carrier paths [18–20]. This model predicts a LMR whose amplitude depends linearly on the carrier mobility and on the guiding center density[18]. Guiding center regions are, however, usually related to local structural defaults or disorder [18,20], which limit the system mobility and hence the amplitude of the resulting LMR to about 200% at 9T [18,19,29]. Other mechanisms inducing local inhomogeneities without affecting the zero-field mobility could therefore lead to a much stronger effect. In particular, magnetically textured regions could lead to local mobility inhomogeneities through magnetic scattering, while potentially retaining high mobility since the crystalline quality would not be affected. More recently, LMR has been observed together with ferromagnetic (FM) order [36] or magnetic signatures (anomalous Hall effect [37,38]), with high amplitudes of about 1000% at 9T. However, tangible evidence of a link between magnetic structure and LMR has yet to be ascertained.

Here we report on a linear positive magnetoresistance in LaTiO₃/SrTiO₃ (LTO/STO) heterostructures with high mobility (up to 40 000 cm² V⁻¹ s⁻¹). The MR amplitude is much higher than in most oxide systems (up to 6500% at 9T), and falls within the range of the colossal magnetoresistance. This linear colossal magnetoresistance is found to be compatible with the Parish-Littlewood theory, with an extremely high coverage of low mobilities regions, between 50% and nearly 90%. Moreover, through low temperature transmission
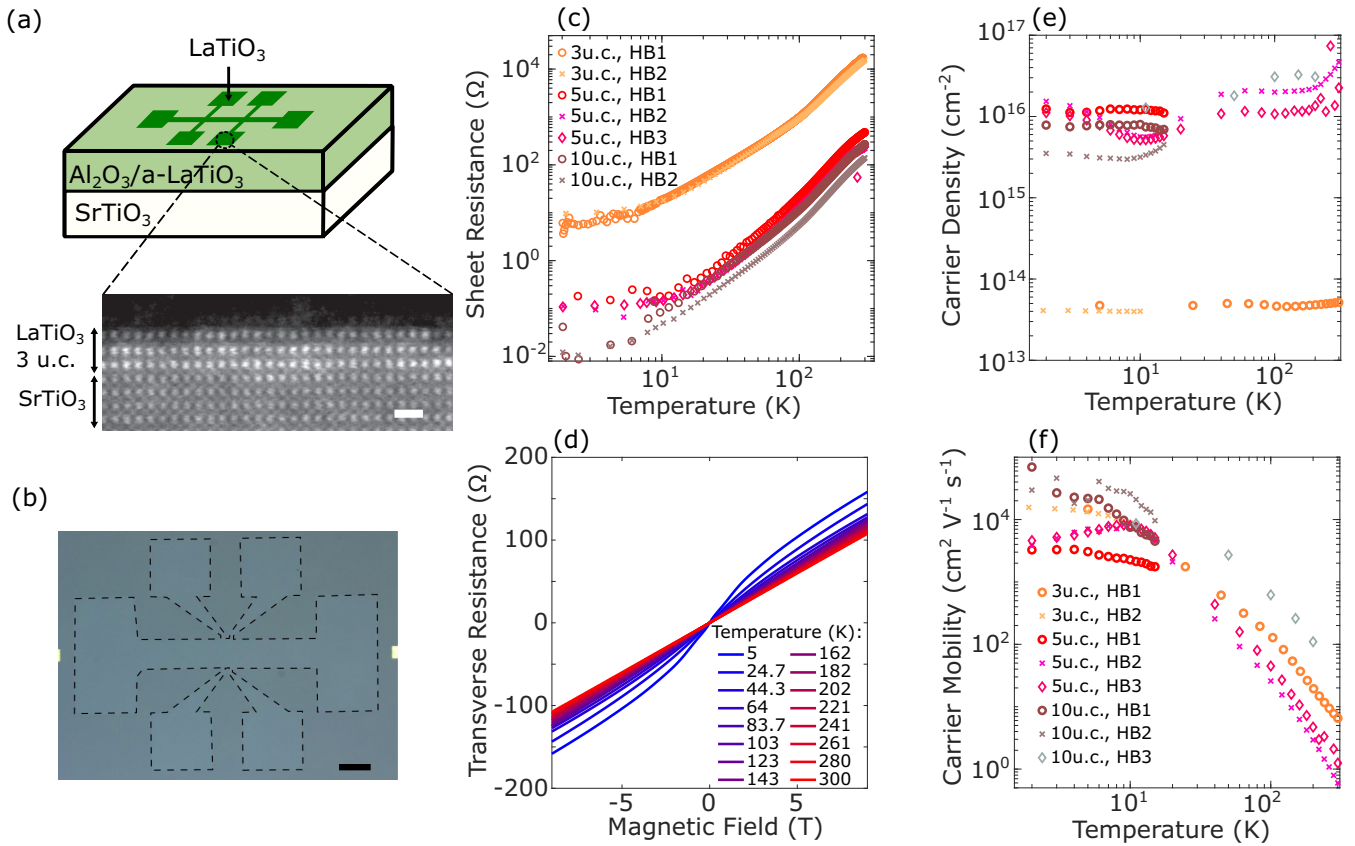
FIG. 1. (a) Top: Schematic of the LTO/STO heterostructures patterned in a Hall bar shape and embedded in amorphous LTO (a-LTO). Bottom: Cross-sectional high resolution scanning TEM image of an LTO 3 u.c. (thickness 1.2 nm) thin film on STO. Scale bar: 1 nm. (b) Optical image of a Hall bar, outlined with a dashed black line. Scale bar: 100 μm. (c) Resistivity versus temperature for different Hall bars (HB) on the 3, 5, and 10 u.c. thick samples. (d) typical Hall effect measurements of the 3 u.c. sample (Hall bar 1) for temperatures ranging from 5 to 300 K. In our experimental configuration, this slope corresponds to electronlike charge carriers. (e) 2D Hall carrier density and (f) mobility of the 3, 5, and 10 u.c. thick samples versus temperature.

electron microscopy (TEM) in magnetic field, we evidence a magnetic uniaxial stripe pattern in the LTO thin film, oriented along well-defined crystallographic axes. Those stripes are compatible with spiral magnetic order in the LTO layer. We suggest those stripes could be related to the low-mobility region and propose a mechanism which could result in the observed colossal LMR. Our work reveals that magnetic texture can induce linear magnetoresistance with colossal amplitude in high mobility devices such as LTO/STO heterostructures.

II. THIN FILM SAMPLES

Our LTO thin films were grown on TiO_2 terminated STO substrates using pulsed laser deposition. The heterostructures where prepatterned with optical lithography similarly to Ref. [39] to achieve crystalline LTO in Hall bar shapes as seen in Figs. 1(a) and 1(b) of different lengths and widths.

We first consider standard transport and Hall characterisation to identify the origin of the main conducting channel. Figure 1(c) shows the temperature dependence of the resistivity for different film thicknesses and Hall bar geometries. The sheet resistance of different Hall bars is well reproducible for a specific film thickness with small variations due to spatial

inhomogeneity of the films. We observe that the sheet resistance decreases significantly from the 3 unit cell (u.c.) to the 5 u.c. film but stays approximately constant for both the 5 u.c. and the 10 u.c. samples. All three investigated thicknesses exhibit clear metallic behavior. The samples further show a high residual resistance ratio $RRR = R(T = 300 \text{ K})/R(T = 2 \text{ K}) \sim 1000\text{–}10\,000$, implying very clean, high quality samples with only trace amounts of impurities and structural disorder. The Hall effect is linear at room temperature, gradually evolving into an s-shape with decreasing temperature [see a typical Hall curve in Fig. 1(d)].

Next we discuss the different conduction channels possible in our LTO/STO heterostructures. Three main channels can be expected: bulk LTO, unintentionally doped STO, and an interface 2D electron system (2DES) between LTO and STO. We first demonstrate through spectroscopy measurements that the LTO layer is conducting. Surface-sensitive x-ray photoemission spectroscopy (XPS) spectra of the Ti 2p core level, recorded at a photon energy of 850 eV, reveal a strong Ti^{4+} signal with a sizable Ti^{3+} admixture, indicating a metallic state of the LTO layer (see Appendix B). This result is further confirmed by angle-resolved photoemission spectroscopy of the valence band with the same probing depth, to check the
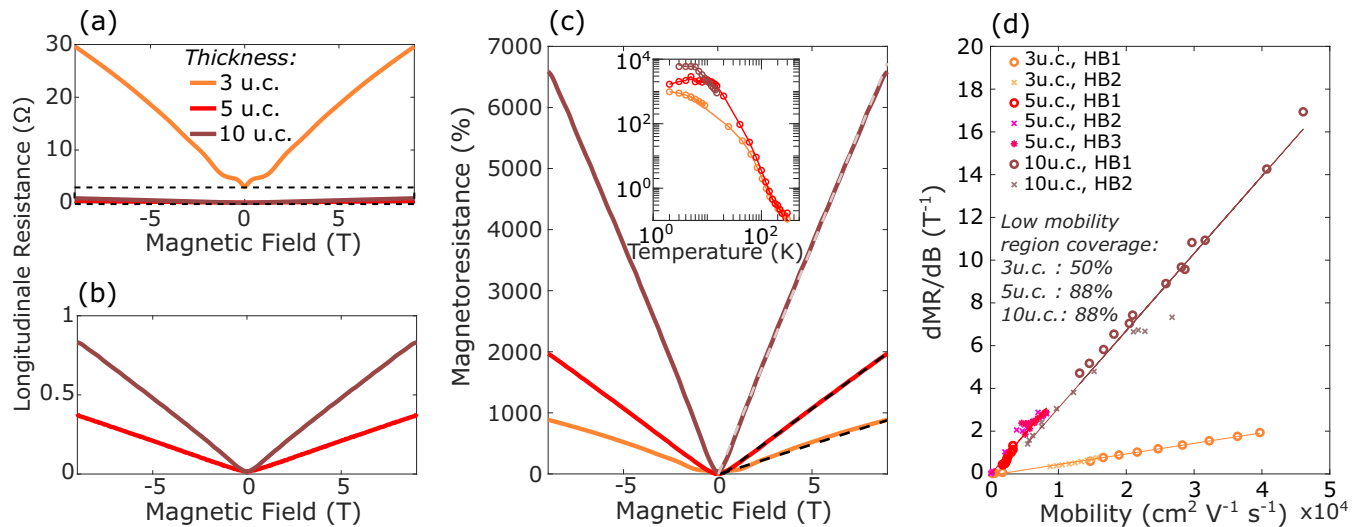
FIG. 2. Magnetoresistance as a function of the perpendicular magnetic field for LTO thicknesses of 3, 5, and 10 u.c. (a) Linear magnetoresistance at $T = 3$K for all three thicknesses and (b) a zoomed in view of only the 5 u.c. and the 10 u.c. samples. (c) Magnetoresistance MR (as defined in the main text) of the samples shown in panel (a) plotted in %. The dashed lines corresponds to a linear fit. Inset: the temperature dependence of the MR in a log-log scale for the three thicknesses at $B = 9$T. (d) Linear slope of the MR at 8T as a function of the mobility of LTO thin films of different thicknesses. Solid lines correspond to linear fits. The areal coverage (in %) of the low mobility regions are extracted from the linear fit.

presence of a Fermi edge (conduction band dispersions) in the LTO film (see Appendix B). With the LTO metallicity now firmly established, we turn to the other possible conduction channels. At high temperature, STO is known to develop oxygen vacancies, which can induce metallicity within a given thickness. Given the high growth temperature, conductivity through the STO can be expected. Finally, a 2DES could be induced at the LTO/STO interface [40]. Therefore, conductivity happens partially in the LTO layer and probably also partially in the STO layer.

The exact LTO thin films' band structure is not well known, nor is the band structure of possible doped STO and interfacial 2DES, so that an unknown number of bands are expected to contribute to transport. Multiband behavior seems confirmed by the observation of the s-shaped Hall effect, a typical sign of multiband transport. Given that the exact number of bands is not known and given the absence of Shubnikov–de Haas oscillations to provide additional information on carrier densities, precise values for each of the carrier densities and mobilities cannot be reliably extracted from a multiband fit of the Hall effect. Instead, we extract the total carrier density n_H from the high field asymptotic slope $(dR_H/dB)|_{9T}$ at 9T of the Hall resistance (R_H), $n_H \simeq 5 \times 10^{13}$ cm^{-2} for the 3 u.c. and $\sim 1 \times 10^{16}$ cm^{-2} for both the 5 and 10 u.c. films at high temperature. These very large charge carrier densities are found to be almost temperature independent as shown in Fig. 1(e). The low temperature variations arise as the Hall effect starts to display nonlinearities. The very high carrier densities are a further indication that part of the transport probably occurs in doped STO. Interestingly, the total transport mobilities [Fig. 1(f)] extracted from the Drude formula as $\mu = \sigma (dR_H/dB)|_{9T}$ (where σ is the conductivity) are found to be up to 40 000 cm^2 V^{-1} s^{-1} at low temperatures reflecting the high sample quality of our heterostructures.

III. LINEAR COLOSSAL MAGNETORESISTANCE

We now turn to an analysis of the magnetoresistance. Figure 2(a) shows the dependence of the longitudinal resistance as a function of the perpendicular magnetic field for Hall bars of different thicknesses studied at 3K. The 3 u.c. sample displays a strong positive MR and further exhibits low-field features that point to Sondheimer oscillations (see Appendix C). The relative increase is even stronger for the 5 and 10 u.c. samples as shown in Fig. 2(b). Furthermore, it can be seen from these measurements that the response is not just colossal but also linear with remarkable precision, starting at magnetic fields well below 1T and with no visible saturation up to at least 11T. All samples studied systematically exhibit this nonsaturating linear magnetoresistance. To better display the relative increase of the resistance, we plot in Fig. 2(c) the MR in % calculated as

$$\mathrm{MR(\%)} = \frac{R(B) - R(B = 0)}{R(B = 0)} \times 100.$$

MR amplitudes of more than 700% at $B = 9$T for the 3 u.c. and up to 6500% at $B = 9$T for the 10 u.c. film are observed, which fall within the range of the colossal magnetoresistance [41]. The MR therefore increases sizably with increasing thickness going from the 3 u.c. to the 10 u.c film. In addition the linear regime sets in for field values that get smaller as the thickness is increased (see Appendix D). This thickness evolution corroborates our conclusion that the transport involves carrier motion in the LTO film.

In the inset of Fig. 2(c) we plot the MR at 9T versus temperature in a log-log scale. The MR amplitude shows a saturation below 10 K and a strong decrease with increasing temperature. In addition, a departure from the linearity is measured for the magnetoresistance and becomes more parabolic-like above ∼60–80 K (see Appendix D).

We see a marked contrast between our findings and those reported for similar LTO/STO heterostructures in Ref. [42] which showed the appearance of Shubnikov–de Haas oscillations starting around 1T and nonlinear magnetoresistance of at most 400% at 9T [42]. The origin of this discrepancy is unclear. Our observation of an LMR is, however, fully reproducible over several samples of varying thickness and several Hall bar geometries. The absence of Shubnikov–de Haas oscillations in our samples despite large transport mobilities, which should allow their observation in our field range, could point to anisotropic scattering in our heterostructures due to strong spin-orbit coupling. This effect can cause the quantum mobility (which determines the onset of the Shubnikov–de Haas regime) to be reduced compared to the transport mobility [43].

The occurrence of LMR has been previously observed in studies on other materials, albeit with significantly reduced amplitude as compared to our results [44–46]. The scenarios that have been proposed to explain the LMR involve either quantum or classical effects. In the case of a quantum origin [1], the linear MR appears in the limit, when all the electrons occupy the lowest Landau level. The MR is calculated as $\rho_{xx} = N_i B / \pi n^2 e$, with n being the carrier density and N_i the concentration of scattering centers. This expression is valid for $B < (\hbar/e)n^{3/2}$ and with an electron density of $\sim 2 \times 10^{23}$ cm^{-3}, the field $B_z = \hbar (3\pi^2 n_e)^{2/3} / 2e$ at which electrons coalesce into a single Landau level is 1×10^5 T [18]. This is far greater than the values in our systems which show an onset well below 1T.

The classical model by Parish and Littlewood, however, describes the origin of the LMR as distortions in the current paths that can be induced by microscopic spatial fluctuations in the carrier mobility [16]. In this model the system is made of low-mobility regions embedded in a high mobility conductor. The stochastic behavior of the electron trajectories around the low-mobility regions tends to induce a counterintuitive transverse motion of the charge carriers around the low-mobility regions at high magnetic field [18]. This transverse motion is in turn responsible for a Hall-like magnetoresistance proportional to the magnetic field [16], which is the LMR [18,20,47]. Such a classical LMR has been observed in highly disordered systems [48] as well as in high mobility systems with weak disorder [49] where the carrier concentration is too high to freeze the electrons in the lowest Landau level (quantum limit). In the Parish-Littlewood theory, at high magnetic field the amplitude of the LMR varies linearly with the average global mobility (determined at zero field), as given by the following equation:

$$\text{MR} = \frac{s}{2L} \mu B, \tag{1}$$

where s is the average radius of the regions, L is the distance between the regions and μ is the mobility.

To validate this scenario in our system, we have plotted the linear slope of the MR curve with respect to the mobility. Thanks to the strong temperature dependence of the Hall mobility in our samples, we can observe the dependence of the LMR slope over a broad mobility range [Fig. 2(d)]. It is clearly seen that the LMR slope depends linearly on the Hall mobility as expected from Eq. (1). Moreover, different

Hall bar geometries with identical thickness consistently fall on the same curve, indicating perfect reproducibility between different samples, also with respect to their inhomogeneity. This linear dependence confirms the presence of low-mobility regions as the origin of the LMR in our samples. Using Eq. (1), we can extract the coverage $s/(s+L) = \frac{1}{1+L/s}$ of these low-mobility islands via the dependence of the slope of the LMR on the mobility (μ). We obtain coverages ranging from 50% for the 3 u.c. sample to 88% for both the 5 and 10 u.c. samples. This is two to six times larger than coverages reported so far [18,19].

The amplitudes of the LMR in our samples are very large for systems with such high coverages of low-mobility regions. The reason for this lies in the combination of both the high background mobility and the substantial coverage of low-mobility regions. As can be seen from Eq. (1), in the guiding centres model, the amplitude of the LMR is proportional to both Hall mobility (μ) and region coverage. In standard thin films and 2DESs, low-mobility regions usually originate from local disorder, whether structural or induced by impurities [18]. As such, an increase in the Hall mobility involves a decrease in the island concentration and conversely. This results in a balance which tends to limit the LMR amplitude. In our system however, we observe both a very high mobility and an exceptional coverage of low-mobility regions. This unusual combination allows us to reach LMR with colossal amplitudes.

However, the combination of very high mobility and large coverage of guiding centres seems incompatible with a structural origin of the low-mobility islands. In the next section, the nature of those low-mobility regions is discussed.

IV. MAGNETIC STRIPE PATTERN

To search for relevant nanometer scale inhomogeneities in the temperature regime where the linear colossal MR is observed, we carried out cryogenic Lorentz transmission electron microscopy (LTEM) on 10 u.c. thick LaTiO$_3$ films. To observe objects in the LTO thin film plane, we used a thinned-down sample as described in Fig. 3(a) and Appendix A. To reveal the nature of the observed LTEM contrast variations, we investigated their dependence on temperature, external magnetic field and defocus at a dedicated continuous-flow liquid Helium-cooled TEM instrument [50].

We first present in Fig. 3(b) a LTEM picture of a typical LTO area measured at low temperature, under zero magnetic field. Only small dark dots distributed across the entire field of view are observed. Those are invariant with temperature and field and may be associated with impurities, precipitates or defects arising from the sample preparation. Under external magnetic field of about 200 mT however, a stripelike uniaxial modulation of the LTEM contrast becomes visible at out-of-focus conditions, as can be seen in the highlighted regions in Fig. 3(c). This stripe pattern is not observed on the whole surface, but only close to bending contours [i.e., loci of locally fulfilled Bragg conditions, which naturally occur in thin strained TEM lamellas, as shown in Figs. 3(a) and 3(c)]. This is not due to the bending causing the stripe pattern, but rather to an amplification mechanism which improves the visibility of low-contrast phase objects close to Bragg
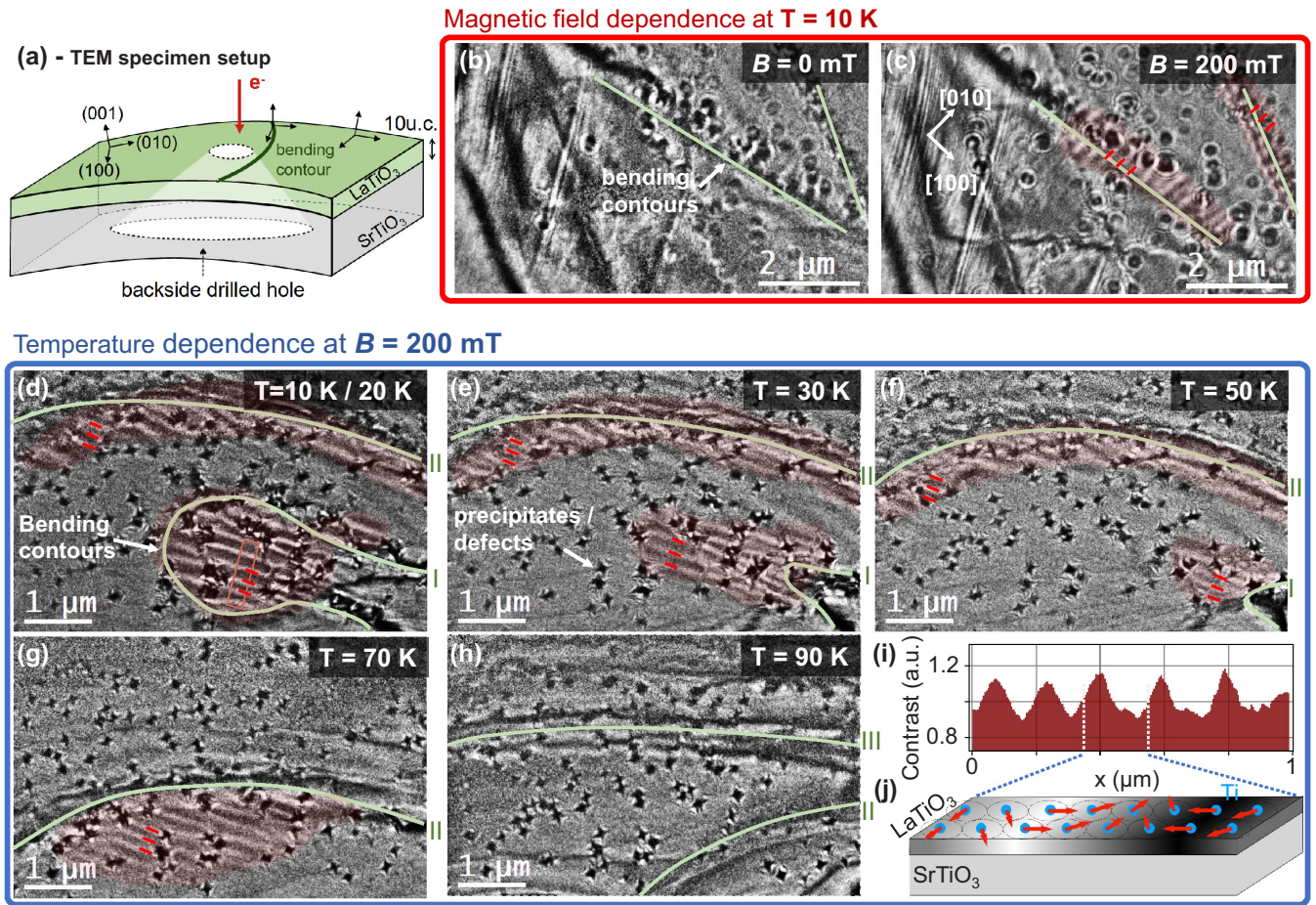
FIG. 3. Temperature- and field-dependent Lorentz transmission electron microscopy (LTEM) of characteristic uniaxial magnetic modulation/texture. (a) Scattering and TEM specimen geometry employed for LTEM. Panels (b), (c) show LTEM images at 10K without magnetic field and with an applied out-of-plane field of 200 mT. The latter exhibits a magnetic texture (highlighted by red shaded areas and red lines) at bending contours (highlighted by green lines), where the direction of modulation agrees with a $\langle 100 \rangle$ crystallographic axis of the cubic $SrTiO_3$ substrate. Panels (d)–(h) show the evolution of LTEM images in a single area at selected temperatures between 10 K and 90 K. The gradual shrinkage and motion of the magnetic texture associated with bending contours I and II with increasing temperature until 90 K is highlighted. Panel (i) displays a line profile along the line scan over the uniaxially modulated region indicated as red arrow in panel (d) revealing a periodicity of about 200 nm. (j) Schematic depiction of the LTEM contrast (one period) by the spin modulation of the Ti atoms.

condition fulfillment, so that the stripes are only visible where a bending contour reveals them (see Appendix E for further discussion of the contrast mechanism). Correlated electron diffraction data further reveals that the modulation direction aligns with the $\langle 010 \rangle$ axis of the underlying $SrTiO_3$ sample (corresponding to the $\langle 110 \rangle$ orientation of the orthorhombic $LaTiO_3$ film), i.e., along the Ti-O-Ti direction [Fig. 3(j) and Appendix E]. To determine the origin of the modulation, we consider its dependence on magnetic field and focus. First, the observed contrast modulation is strongly field dependent and virtually vanishes at zero external field [Figs. 3(b) and 3(c)]. Moreover, the contrast vanishes in focus and changes sign upon inverting the sign of the focus (see Appendix E). These observations are compatible with the presence of a uniaxial magnetic texture in the $LaTiO_3$ films. To our knowledge, the existence of such a magnetic structure has not been previously reported in $LaTiO_3$.

To investigate the stability of the magnetic stripe texture, we performed temperature dependent measurements.

Figures 3(d)–3(h) present the evolution of LTEM images of a particular LTO area at different temperatures. As temperature changes, the bending contours (labeled I, II, and III) and the stripes they reveal, shift. The stripes appear stable between 8 and 20 K. Above 20 K they start to disappear, where the shrinking of the modulated regions may be inhomogeneous. For instance, stripe modulations associated to bending contour I seems to be gone at around 35 K (not shown), whereas that associated to contour II persists up to 80 K. At 90 K, no stripes are visible anymore [see Fig. 3(h)]. By analyzing a line-cut of the contrast profile averaged in the red box in Fig. 3(c), we observe that the modulation has a periodicity of 188 ± 16 nm within the resolution of our measurement [Fig. 3(i)]. We observe no clear temperature dependence of the periodicity of the modulation.

Owing to the unique contrast amplification mechanism, which makes the stripes only visible around the bending contours, we cannot determine the fractional coverage of the modulation. However, the apparently continuous shifting of

the modulation with bending contour II in Figs. 3(d)–3(g) indicates a very large part of the observed area, of several tens of percent, is covered by stripes.

V. DISCUSSION

The uniaxial magnetic texture in the LTO film observed in LTEM covers a sizable area of the sample with a morphology that evolves with temperature above 20 K up until 80 K when the pattern disappears. These features are very similar to those ascribed to the low mobility regions in magnetotransport. In the following we discuss a possible origin of the magnetic texture as well as its impact on magnetotransport.

Magnetic stripes were reported in STO-based heterostructures, originating from ferroelastic domain walls in STO substrates [51,52]. These domains however have typical sizes ranging from 5 to 15 μm [51,52], which is more than one order of magnitude larger than those we observe. This casts some doubt on their role to explain our modulation. Experimental [53] and theoretical [54] investigations established that bulk LaTiO$_3$ orders antiferromagnetically (AF) at low temperature with canted Ti^{3+} moments owing to orthorhombic distortions, resulting in a small ferromagnetic component. Another possible explanation for the uniaxial modulation would then be ferromagnetic stripes with out-of-plane anisotropy. However, this scenario would imply out-of-plane magnetic domains separated by Bloch-like domain boundaries [55], both of which would generate no contrast in our LTEM configuration.

Based on the large Rashba spin-orbit coupling of the LTO thin film [42], we propose an alternative scenario where a spiral magnetic phase is stabilized by the double exchange process between mobile carriers and static moments, owing to a large Hund's coupling energy [56,57]. According to the double exchange scenario, the spins $\mathbf{S_{\tilde{r}}}$ of the mobile carriers are locked to the local Ti^{3+} magnetic moments. The ground state is determined by a balance between an effective exchange term $J \sim t n_f$ (with t the hopping energy and n_f the mobile electronic fraction per Ti atom), a Dzyaloshinskii-Moriya (DM) term $D \sim \alpha n_f$ (where α is the interfacial Rashba-like spin-orbit energy) and an exchange anisotropy term A [56,57]. The corresponding effective spin Hamiltonian reads

$$\mathcal{H}_{\text{eff}} = \sum_{\tilde{\mathbf{r}}} -J(\mathbf{S_{\tilde{r}}} \cdot \mathbf{S_{\tilde{r}+\hat{x}a_0}} + \mathbf{S_{\tilde{r}}} \cdot \mathbf{S_{\tilde{r}+\hat{y}a_0}}) - D\hat{\mathbf{z}} \cdot \mathbf{S_{\tilde{r}}} \times \mathbf{S_{\tilde{r}+\hat{Q}a_0}}$$
$$- A S^y_{\tilde{r}} S^y_{\tilde{r}+\hat{x}a_0} - A S^x_{\tilde{r}} S^x_{\tilde{r}+\hat{y}a_0}, \qquad (2)$$

where $\hat{\mathbf{z}}$ corresponds to the out-of-plane [001] direction, $\mathbf{a_0}$ is the in-plane Ti-O-Ti distance, and $\hat{\mathbf{x}}$ and $\hat{\mathbf{y}}$ denote the Ti-O-Ti bond directions (see Appendix F for further details). For the set of parameters relevant to the LTO/STO interface ($t \sim 250$ meV [58], $\alpha \sim 2$ meV [59]), the ground-state configuration is a spiral, propagating with a wavevector $Q = \frac{2D}{Ja_0}$ parallel to the Ti-O-Ti bonds ($\langle 100 \rangle$ or $\langle 010 \rangle$ direction in the pseudocubic LTO frame) and polarized in a plane parallel to the interface [56,57]. Here, in contrast to the LaAlO$_3$/SrTiO$_3$ interface case when the DM term is in-plane, octahedral rotations in LTO/STO allow an out-of-plane DM contribution. This is important in our case since only an in-plane spiral [like the one schematically presented in Fig. 3(j)] would result in a LTEM contrast. We calculate the pitch of

Magnetic spiral domain: low mobility region

LaTiO$_3$

Possible 2DES

SrTiO$_3$

e$^-$

Higher-mobility LaTiO$_3$ regions, high-mobility possible 2DES and doped STO
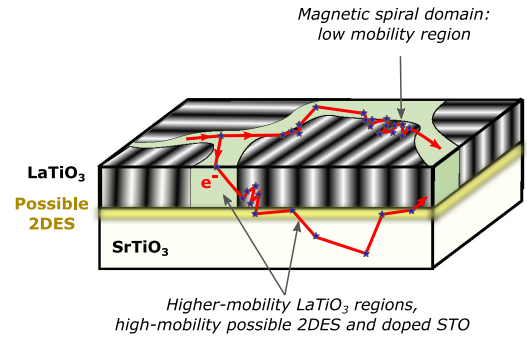
FIG. 4. Schematic view of electronic transport in magnetic LTO/STO heterostructures in the Parish-Littlewood framework. Spiral magnetic domains (represented by stripes) are associated with increased magnetic scattering, leading to lower mobility. In LTO regions which are not in the spiral ground state (light green), or a possible 2DES (yellow), magnetic scattering is reduced, leading to higher mobility. Doped STO is also known to exhibit high mobility.

the spiral to be $\mathbf{d} = \frac{2\pi}{Q} \sim 160$ nm. Both the pitch and the modulation direction are in good agreement with our LTEM measurements.

We now consider the relationship between LMR and magnetic spiral magnetic texture. In STO-based heterostructures, LMR is often interpreted in terms of the Parish-Littlewood model [19,31,37,60,61], but usually without a clear picture of the low-mobility regions' nature, usually attributed to structural disorder [31,37,60,61]. It was recently proposed that magnetism could also be responsible for the mobility inhomogeneities [37]. In our LTO/STO heterostructures, the existence of the magnetic spiral state in LTO can strongly influence magnetotransport. In particular, in the magnetic region, magnetic scattering can significantly increase the scattering rate. Considering that a spin-spiral texture consist of successive interfaces between magnetic slabs with small tilt of the magnetization between them, we estimate that the scattering rate in the spin-spiral domains is more than one order of magnitude larger than in the rest of the sample (see Appendix F). In the framework of the Parish-Littlewood scenario discussed in the linear magnetoresistance part [16,18], we propose that the low-mobility regions could correspond to the magnetic regions of the LTO film, where electrons would experience spin-scattering. This would naturally explain the high calculated coverage. Figure 4 shows a simplified schematic picture of the electronic transport through the different regions of the heterostructure. The high-mobility channels could be composed of either nonmagnetic LTO regions, of a confined 2DES or unintentionally doped STO layer, where the high-mobility would not be impacted as much by magnetic scattering. Since the proportion of LTO in the total conducting volume only increase with film thickness, the low-mobility region coverage would also increase with thickness, as is observed. Compared to the two-dimensional case considered in the Paris-Littlewood model, the 3D case of our LTO/STO heterostructures is more complex due to the charge carriers' motion in the out-of-plane direction and in-between conducting channels. The exact influence of a three-dimensional electron motion within the heterostructure on the Parish-

Littlewood theory is unclear, and should be further examined theoretically.

VI. CONCLUSION

To summarize our findings, $LaTiO_3$ thin films on $SrTiO_3$ were investigated using magnetotransport and transmission electron microscopy measurements. The main result is the observation of a nonsaturating linear magnetoresistance of the heterostructures, with a colossal amplitude up to 6500% at 9T. This very large effect is understood as resulting from the combination of high carrier mobility (40 000 $cm^2\,V^{-1}\,s^{-1}$) with an extreme coverage of guiding-centre regions of 49% up to 89%. We propose that these lower-mobility regions are tied to a striped pattern of magnetic origin in the $LaTiO_3$ film revealed by Lorentz TEM. The observed striped pattern is shown to be compatible with spiral magnetism. Our study establishes a possible link between nonsaturating linear colossal magnetoresistance and complex magnetic structure. This result suggests a new design concept for devices with large linear magnetoresistance in magnetic materials and heterostructures. We further expect it to trigger further theoretical interest on linear magnetoresistance in inhomogeneous and magnetic systems.

APPENDIX A: EXPERIMENTAL SECTION

1. Growth

For growth a laser flux of 1.5 J cm^{-2} and a polycrystalline $La_2Ti_2O_7$ target at a distance of 55 mm from the substrate were employed. Thin films with different thicknesses of 3, 5, and 10 unit cells (u.c.) were grown into Hall bars designs, with lengths of 20, 40, 60 and 80 μm and widths of 50, 100 and 150 μm, using a similar method as described in Ref. [39]. A negative mask of Al_2O_3 was first deposited onto a STO substrate prior to PLD growth. As a result, LTO grows epitaxially on STO in Hall bar-shaped trenches, while growing amorphous onto Al_2O_3. In the text, all Hall bars of a given thickness presented are located on a single grown LTO/STO thin film. During growth, the band filling of LTO can be tuned by excess oxygen doping [62]. All samples investigated were grown under an oxygen background pressure of 1×10^{-6} mbar, inducing over oxidation and thus producing a correlated metallic system. The growth temperature was 800°C for all samples. The samples were glued to chip carriers and wire bonded for the magnetotransport measurements.

2. Transport measurements

Magnetotransport experiments were performed using a Quantum Design physical properties measurement system (PPMS) in pseudo-AC mode, and with a ^{3}He − ^{4}He dilution refrigerator with the magnetic field applied perpendicular to the films, using standard lock-in techniques. The transverse magnetoresistance (MR) was studied with magnetic fields up to 11T, generated by a superconducting magnet. In Figs. 1 and 2, several Hall bars of different sizes are investigated: Hall bars 1 are 20×50 μm, Hall bars 2 are 20×80 μm, and Hall bars 3 are 50×150 μm.

3. TEM preparation and measurements

Electron-transparent TEM samples have been prepared by a classical back-side thinning procedure consisting of (A) manual coarse mechanical grinding, (B) dimpling, and (C) final Ar ion milling using a precision ion polishing system (PIPS 691, Gatan Inc., U.S.) until a hole appears. All thinning steps have been applied from the back (substrate) side of the sample to preserve the $LaTiO_3$ film. The latter was verified by employing TEM-EDX, which showed the presence of La throughout the entire sample region of interest. Cryogenic TEM investigations were carried out at the JEOL 2010F Dresden special instrument [50] operated at an acceleration voltage of 200 kV. The microscope is fitted with a custom-made continuous-flow liquid Helium cryostat enabling stable cooling for several days while varying temperature, which is essential for the above studies. External magnetic fields were applied by exciting the objective lens coils of the TEM. Lorentz imaging (i.e., out-of-focus and small external field conditions) was set by varying the first transfer lens (TL11) of the CETCOR imaging corrector utilized as a pseudo Lorentz lens. The defocus in the field series (Fig. 3) as well as in the focal series (see Appendix E) was adjusted by inspecting the diffraction (Fresnel fringes) at the sample edge. The background of the TEM images in Figs. 3(b)–3(h) due to thickness variations of the wedge-shaped sample [see Fig. 3(a)] was subtracted to enhance the magnetic contrast.

APPENDIX B: GROWTH AND SPECTROSCOPY

The film thickness and quality is probed by reflection high energy electron diffraction (RHEED), exemplarily depicted for the 5 u.c. $LaTiO_3$ (LTO) film from the main manuscript in Figs. 5(a)–5(c). The diffraction pattern of the LTO film stays the same as the substrate indicating growth fully strained to the substrate. At room temperature, the lattice mismatch between LTO and $SrTiO_3$ (STO) is 1.74%, while below the tetragonal transition of STO it increases to 1.8%. The intensity of the specular spot is monitored during growth to determine the film thickness. Each oscillation corresponds to a completed LTO layer. Due to the lithographic process, during which large areas of the bare substrate are covered with amorphous Al_2O_3, the following low-energy electron diffraction (LEED) and photoemission spectroscopy data is taken
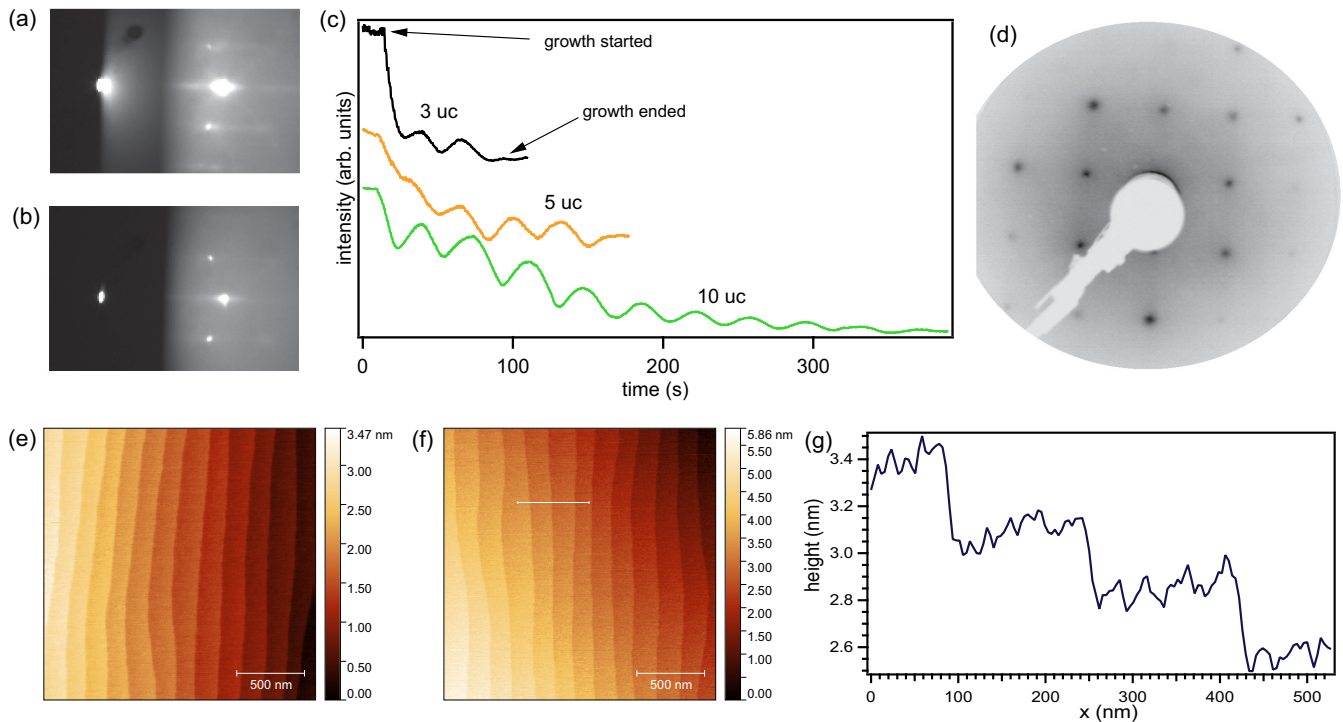
FIG. 5. Film growth and characterization. (a) RHEED pattern of the bare substrate, (b) RHEED pattern of the completed 5 uc $LaTiO_3$ sample, and (c) RHEED intensity of the specular spot during growth for a 3 u.c., a 5 u.c., and a 10 u.c. sample. Each oscillation corresponds to a completed unit cell layer. (d) LEED image of the film surface at a electron kinetic energy of 120 eV. The clean 1×1 reconstruction is imposed by the STO substrate. (e) AFM image of the bare substrate. (f) AFM image of a 5 u.c. $LaTiO_3$ film, with (g) a line profile. Large flat terraces with unit cell high steps of roughly 4 Å are visible.

on a non patterned reference sample, as the measurement area of these methods eclipses the pattern size significantly. The LEED image in Fig. 5(d) confirms the high crystalline quality of the LTO film especially at the film surface. The 1×1 diffraction pattern is imposed by the $SrTiO_3$ substrate.

The TiO_2 terminated substrates possess large flat terraces with unit cell high steps as can be inferred from the atomic force microscope image in Fig. 5(e). Another indicator for the high quality of the LTO films is, that their surfaces are barely discernible from the substrate in AFM, as demonstrated in the image of a 5 u.c. film with line profile in Figs. 5(f) and 5(g).

The electronic state of the samples is independently investigated by photoemission spectroscopy on samples in the same state as the transport samples. Using soft x-rays at the Ti L_3 edge ($h\nu = 461.5$ eV) we probe the valence band region as can be seen in Fig. 6(a) for a 3 u.c. LTO sample. At the Fermi energy a quasiparticle peak and just 1.1 eV below it the lower Hubbard band are observed. The observation of the former in particular indicates metallic behavior. Due to the very limited inelastic mean free path of the photoelectrons at this excitation energy (approximately 1 nm according to Tanuma *et al.* [63]) and a film thickness of 1.2 nm, we can conclude, that the LTO film itself and possibly the interfacial $SrTiO_3$ layers are metallic. Additionally we present in Fig. 7 a bandmap along the Γ-X direction taken at 461.5 eV photon energy. Bright dispersing bands at the Γ points are clearly visible. Note that the stripelike artifacts are caused by a mesh in the used wide angle acceptance lens. As measurements at this photon energy are sensitive predominantly to the LTO layers, this

experiment is a further indicator for metallicity of the LTO layers. The most likely explanation for that metallicity appears to be excess oxygen *p*-doping [62].

To check this hypothesis we also analyze the Ti $2p$ core level by x-ray photoemission spectroscopy at a photon energy of $h\nu = 850$ eV. This photon energy was chosen so that the kinetic energy and thus the inelastic mean free path of the photoelectrons and the information depth remains the same as in the valence band spectrum. As can be seen in Fig. 6(b) for the same 3 uc LTO sample from above, the spectra are dominated by the Ti^{4+} valency, indicating a trivial insulating Ti $3d^0$ configuration. Nonetheless significant Ti^{3+} spectral weight, chemically shifted to lower binding energies is observed, which we would expect for stoichiometric LTO and which is indicating the presence of Ti $3d$ electrons. The coexistence of both valencies confirms the suspicion that the $LaTiO_3$ is grown overoxidized as $LaTiO_{3+x}$. To determine the x is not easy, as the $SrTiO_3$ substrate also contributes a small exponentially dampened Ti^{4+} signal, and—in the not unlikely scenario of oxygen vacancies in the substrate—also an even smaller Ti^{3+} signal to the spectra. The second spectrum recorded at an emission angle of 25° off normal emission was taken to artificially reduce the effective inelastic mean free path and thus probe the homogeneity of the Ti valency distribution. The lack of angle dependance of the Ti^{3+} to Ti^{4+} ratio indicates a homogeneous mix of the valencies throughout the probed depth and thus a homogeneous spread of the conducting Ti $3d$ electrons. If only a conducting interface or interfacial $SrTiO_3$ would harbor Ti $3d$ electrons, only there would Ti^{3+} valency
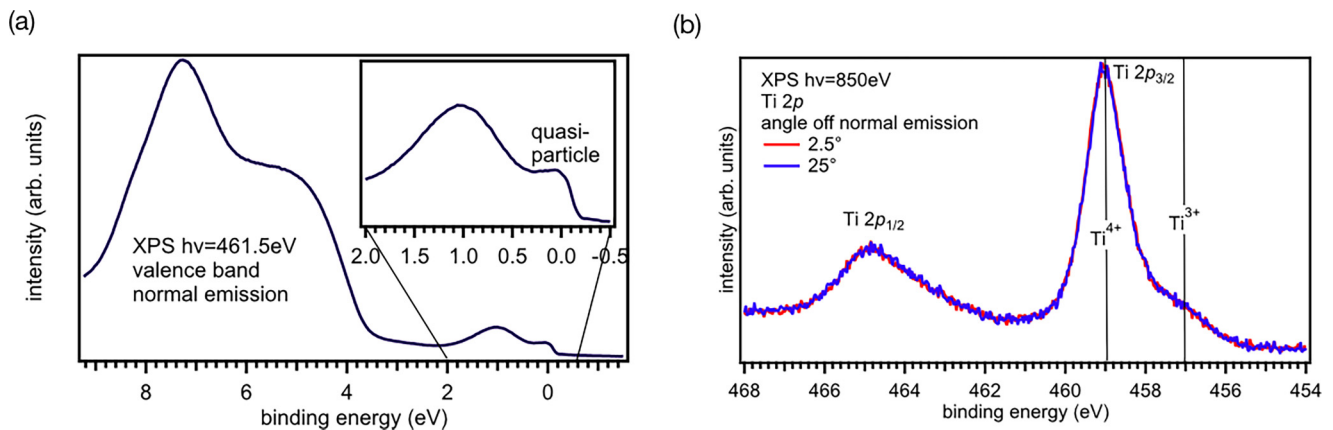
(a)

(b)

FIG. 6. X-ray photoemission spectroscopy. (a) X-ray photoemission spectrum of the valence band region with zoom in on the Ti $3d$ containing region just below the Fermi energy. The quasiparticle spectral weight indicates metallic behavior of LTO. (b) X-ray photoemission spectra of the Ti $2p$ core level, taken at emission angles 2.5° and 25° off normal emission and a photon energy of 850 eV. Intensity is normalized to integral of the Ti 2p spectral weight. The spectra at both emission angles are heavily dominated by the Ti^{4+} valency.

be expected and thus a strong angle dependence of the Ti^{3+} to Ti^{4+} ratio would be observed.

APPENDIX C: SONDHEIMER OSCILLATIONS

In 3 u.c. thick LTO/STO samples, low-field oscillations were systematically observed [see Fig. 8(a)]. Due to their small amplitude, those oscillations are more visible in the second derivative of the resistance [see Fig. 8(b)]. These oscillations are visible at low field, starting from zero field on. Their amplitude is damped with increasing magnetic field, and the oscillations finally disappear above about 4T. The amplitude also decreases in amplitude while temperature is increased, and completely vanishes above about 13 K.

The fact that the oscillations exist only at low field and are damped with magnetic field is at odds with that of Shubnikov–de Haas oscillations, which are often observed in high-mobility thin films but would appear starting from a finite field and increase in amplitude with increasing field. Moreover, the peak position increases linearly with magnetic field, as shown in see Fig. 8(c), with a periodicity of ~1T. This further

discounts a Shubnikov–de Haas origin of these low-field oscillations, which would be periodic in inverse magnetic field.

A possible explanation for those oscillations are the so-called Sondheimer oscillations. They are semiclassical oscillations that are due to a resonance condition between cyclotron radius r_c and thickness of the thin film t. When applying a transverse magnetic field to a metallic thin-film, electrons undergo cyclotron orbits in plane, which added to the out-of-plane velocity creates a helical motion. If the mean free path l_e is larger than the film thickness, full helical motion can occur within the film thickness without scattering. The number of cyclotron revolution of the trajectory in the thickness is $n = \tau_z/\tau_c$, with $\tau_z = t/v_z$ the time to propagate in the film thickness from one interface to the other (v_z is the velocity in the out-of-plane direction); and $\tau_c = \frac{2\pi}{\omega_c}$ the time to close a cyclotron orbit in-plane (ω_c is the cyclotron pulsation). When n is an integer, no net in-plane motion is made while propagating in the thickness. However, when n is noninteger, the helix trajectory is interrupted at the film interface, resulting in a net in-plane motion. As Sondheimer showed, this results in an oscillatory behavior of the resistance with magnetic field, where oscillations occur with period $\Delta B = \frac{\hbar}{et} \frac{\partial A}{\partial k_z}$ [64–66]. Here $\frac{\partial A}{\partial k_z}$ corresponds to the derivative of the cross-section of the Fermi surface A with out-of-plane momentum k_z.

The fact that the observed oscillations are periodic in B, along with the fact that the first oscillation occurs at a smaller field than the 1T periodicity [see Fig. 8(c)], is compatible with the Sondheimer explanation [64]. The extraction of further information about the electronic structure of the film would however require additional information about the band structure and effective mass of the charge carriers, which are unavailable due to the absence of Shubnikov–de Haas oscillations.

APPENDIX D: TEMPERATURE AND FIELD DEPENDENCE OF THE LINEAR MAGNETORESISTANCE

To determine the onset field of the linear magnetoresistance, we plotted the magnetoresistance in a log-log scale
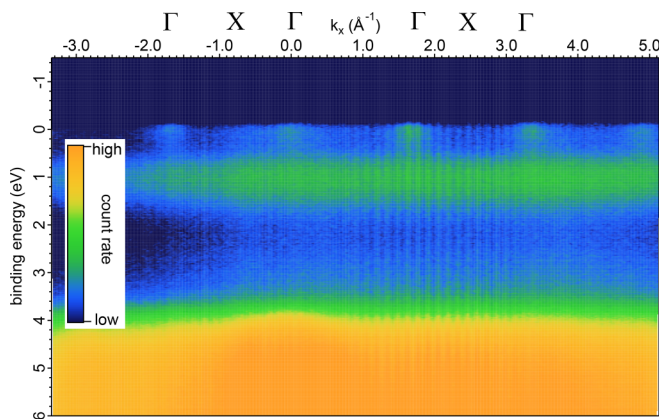

FIG. 7. Photoemission spectroscopy. Γ-X band map of the same sample as in Fig. 6 taken at 461.5 eV.
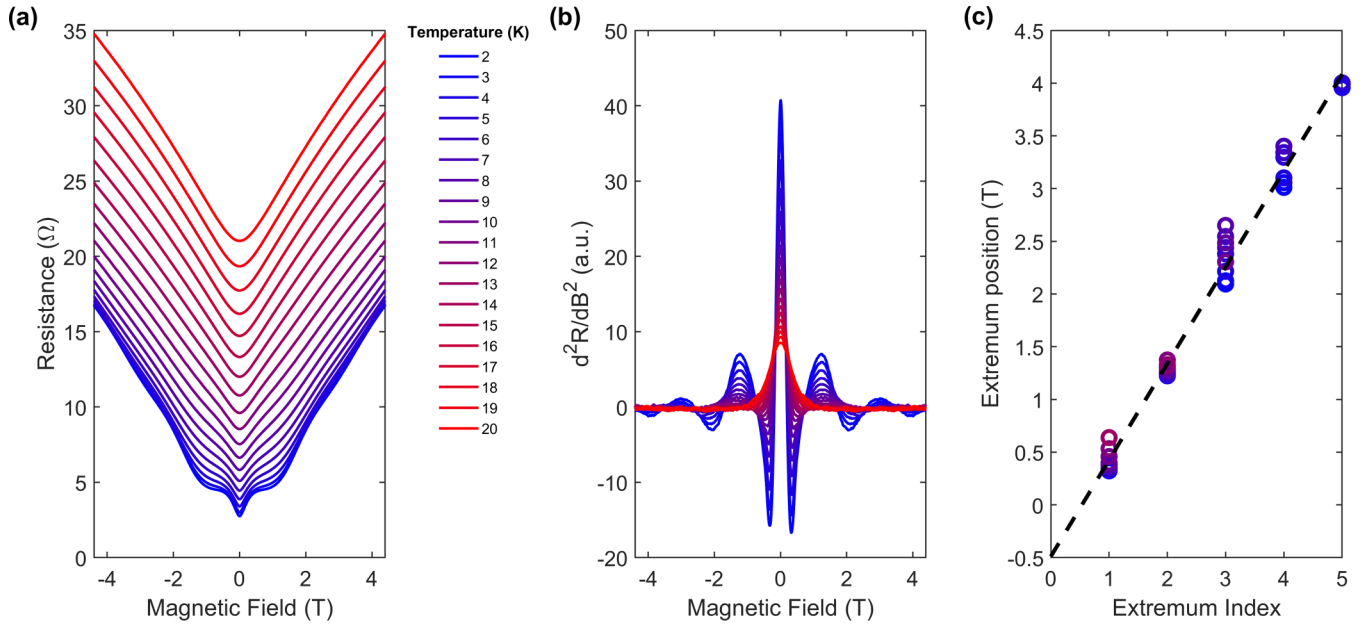
FIG. 8. Sondheimer oscillations in 3 u.c. samples. (a) Raw longitudinal magnetoresistance at several temperatures. (b) Second derivative of the longitudinal magnetoresistance in panel (a), revealing oscillations around zero field at low temperature. (c) Indexed peak position of the oscillations. The linear dependence of the peak position with magnetic field reveals the Sondheimer origin.

in Fig. 9. The linear slope in the log-log plot correspond to the linear MR behavior. An estimate of the critical field at which magnetoresistance becomes linear is defined as the intersect between linear fit and zero-field value. We observe that the critical field decreases with increasing thickness. At low temperature, for the 3 u.c. sample, this field is close to 1T, while it decrease in the 5 u.c. sample to 500 mT, and to less than 200 mT for the 10 u.c. sample (see Fig. 9).

The linear magnetoresistance studied in the main text is a low-temperature effect. To illustrate this, we plotted in Fig. 10

the normalized magnetoresistance

$$\mathrm{MR_{norm}} = \frac{R(B,T) - R(0\mathrm{T},T)}{R(9\mathrm{T},T) - R(0\mathrm{T},T)}.$$

This allows one to observe the transition from a very linear behavior to a parabolic-like behavior. This transition is evidenced in Fig. 10 by the linear fit at low temperature (dashed line) and the parabolic fits at high temperature (dotted line). For the 3u.c. sample, the transition between both regimes accelerates above 30–40 K, which corresponds to the
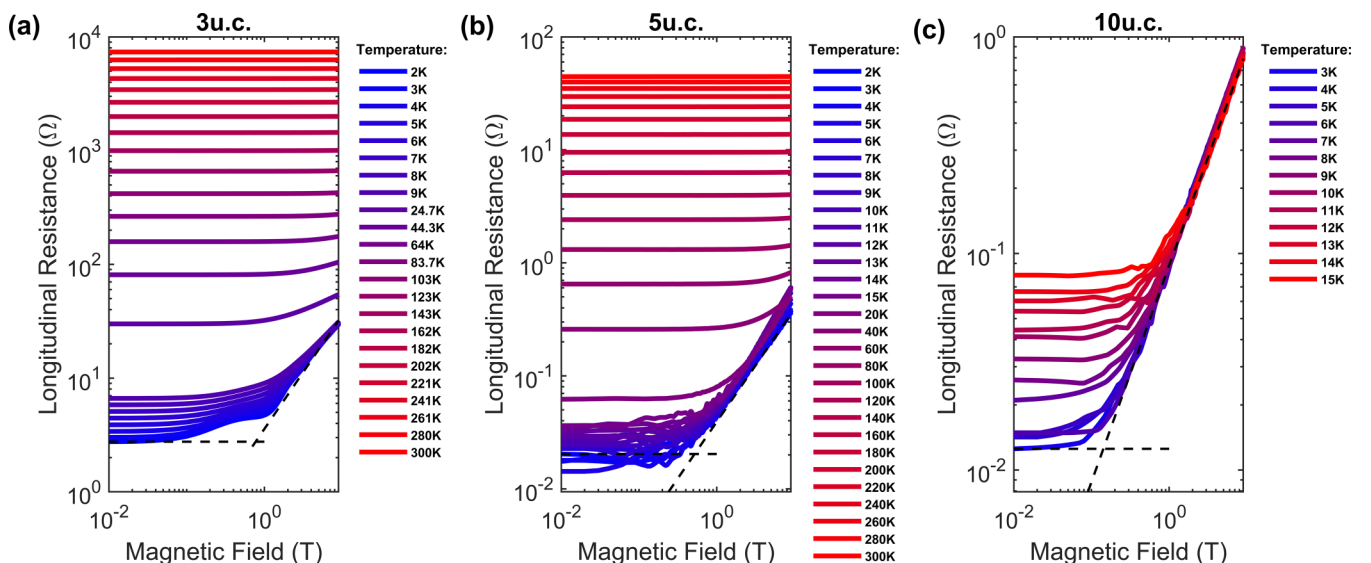

FIG. 9. Magnetoresistance in log-log scale for samples of all three thicknesses. For each thickness [(a) 3 u.c., (b) 5 u.c., (c) 10 u.c.], curves at different temperatures are shown. Dashed lines show linear fits of the lowest temperature data and the intersect with zero-field value.
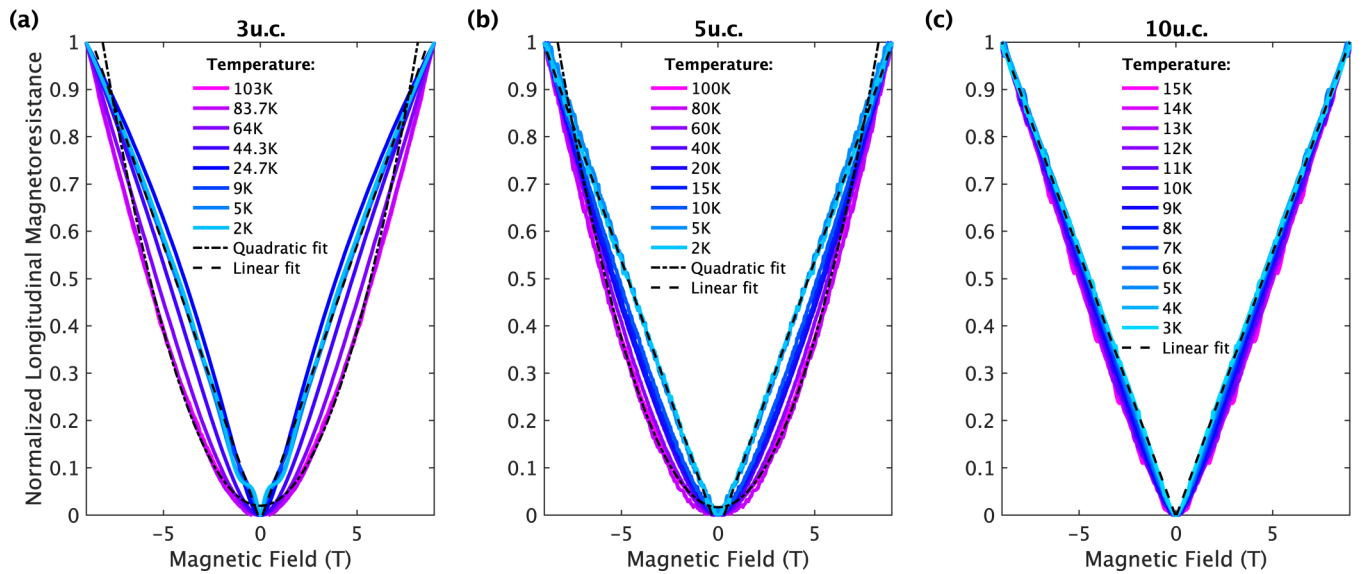
FIG. 10. Normalized magnetoresistance at various temperatures for samples of all three thicknesses, same as in Fig. 9. For each sample [(a) 3 u.c., (b) 5 u.c., (c) 10 u.c.]. Dashed lines are linear fit, and dotted lines are parabolic fits. The transition between linear and parabolic-like behavior occurs around ∼40 K for the 3 u.c. and the 5 u.c. samples.

temperature at which the magnetic stripe pattern observed in cryogenic TEM starts to vanish. For the 10 u.c. sample, the magnetoresistance remains linear up to the maximum temperature of 15 K.

APPENDIX E: LORENTZ TEM IMAGING

In this Appendix, we supply images of the uniaxial modulation acquired at different foci (Fig. 11). They illustrate the fact that the modulation contrast vanished in focus and changes sign going from under- to overfocus, which proves that the observed contrast is a phase contrast (i.e., stems from a phase modulation of the complex electron wave only). Such a modulation typically indicate magnetic textures in the sample. An electric origin (e.g., ferroelectric domains) is ruled out in this case due to the strong magnetic field dependence of the modulation. The small dark dots distributed across the entire field of view may be associated to impurities, or point defects.

They are deformed to asterisks due to induced astigmatism caused by the applied external magnetic field.

Note, however, that the small film thickness of the LTO shifts the phase modulation below observability threshold in standard kinematic scattering conditions employed in Lorentz TEM. Typical Lorentz TEM observations of such modulations require magnetic film thickness of several tens of nanometer. As mentioned in the main text, to reveal the magnetic stripes in our thin films we exploit the enhanced sensitivity of dynamic scattering conditions (i.e., scattering beyond first order Born approximation valid close to locally fulfilled Bragg conditions for electron diffraction) toward small phase shift (equivalent to scattering direction) modulations of the electron beam [67] imprinted by magnetic fields in the thin LaTiO$_3$ film [Fig. 3(a) of the main text]. Close to Bragg conditions, where scattering into systematic diffraction directions is strongly enhanced and dynamical scattering sets in (exemplified by the loss of intensity in bending contours of nondiffracted beam), small phase (and corresponding beam
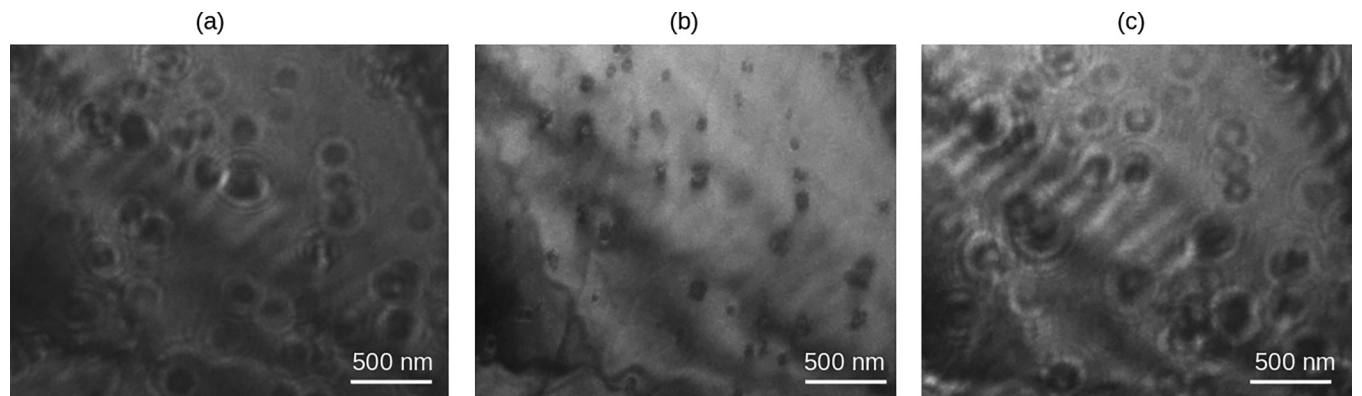

FIG. 11. LTEM images of LTO sample region depicted in Figs. 3(b) and 3(c), (a) underfocus, (b) in focus, and (c) overfocus. Stripe contrast is inverted going from under- to overfocus and consequently vanished in focus.
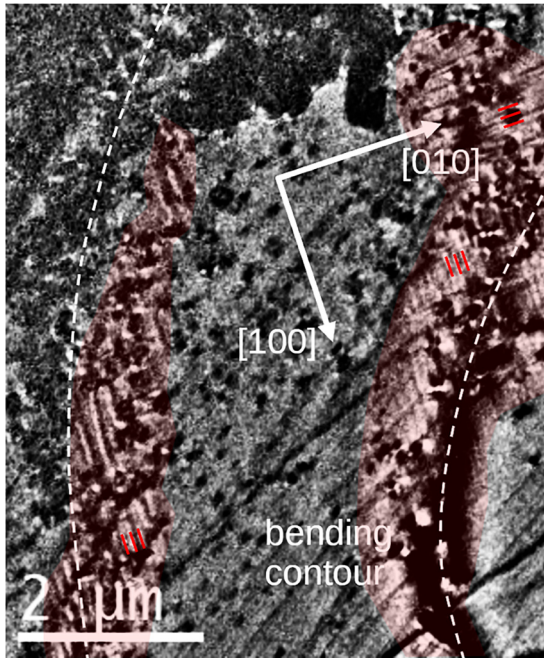
FIG. 12. Perpendicular uniaxial stripe modulations aligned with crystal axis orientations of SrTiO$_3$. The striped areas are highlighted with red shading and the stripes with red lines.

FIG. 13. Magnetic moments (yellow arrows) on the four primitive Ti^{3+} ions in the LaTiO$_3$ structure. They are labeled 1-2-3-4. Ti atoms are shown in blue, O atoms in red, and La atoms in green.

direction) modulations can be magnified by more than one order of magnitude depending on the excitation error (i.e., deviation from exact Bragg condition) and other parameters like the thickness of the sample. This is sufficient to amplify the small magnetic phase modulation of the thin LTO film in our case. These are then visualized under strong defocus (LTEM imaging conditions).

Lastly, we provide in Fig. 12 another example of uniaxial stripe modulations at bending contours, which exhibit two perpendicular modulation directions aligned with the crystallographic orientations of the underlying SrTiO$_3$ substrate in one field of view.

APPENDIX F: THEORETICAL MODELING

1. Magnetism in the LaTiO$_3$ heterostructure

Experimental [53] and theoretical [54] investigations established that bulk LaTiO$_3$ orders antiferromagnetically (AF) at low temperature with canted Ti^{3+} moments, resulting in a small ferromagnetic component. The structure is shown in Fig. 13, where (a, b, c) refers to the orthorhombic basis vectors. $\theta \sim 1°$ is the angle of the magnetic moments with respect to the (a, b) plane and $\phi \sim 1.4°$ denotes the absolute value of the angle between the projection of the moments onto the (a, b) plane and the a axis. The canted AF ordering is caused by Dzyaloshinskii-Moriya (DM) and exchange asymmetry terms allowed by symmetry. Doping the system with holes leads to a percolative-style decrease in the magnitude of the zero temperature average moment as observed in experiments on LaTiO$_{3+\delta}$ samples with $0 \leqslant \delta \leqslant 0.08$ [53]. At low temperature, a metal-to-insulator transition occurs at a critical doping $\delta \sim 0.05$ such that the material is insulating for $\delta < 0.05$, while it hosts coexisting metallic and magnetic
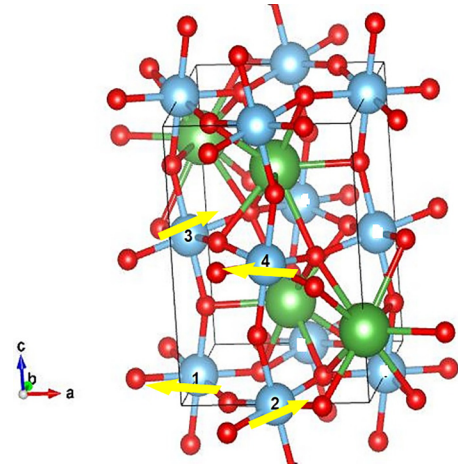
states for $\delta > 0.05$. The off-stoichiometry oxygen holes dope the Ti ions turning a fraction of them into Ti^{4+}. This causes site dilution of the magnetic Ti^{3+} moments and also produces metallic puddles. When $\delta \sim 0.05$ puddles merge to form a percolative metallic phase [68]. When $\delta > 0.08$ a homogeneous metallic and paramagnetic state is obtained.

The LTO/STO heterostructure is polar and to mitigate the electrostatic energy build-up [69] an electron liquid is produced in the material. If we consider that the negative charges originate from the Ti^{3+} ions on the LTO side, we may transpose the previous considerations to the interface case. We note that, in contrast to the LaAlO$_3$/SrTiO$_3$ case, metallicity is expected to concern both sides of the interface. If the uniaxial modulations observed in TEM are caused by a spiral magnetic structure, as we argue in the main text, we conclude that in our experiments, the electron fraction n_f donated by each Ti^{3+} site of LTO in the heterostructure is such that $0.1 < n_f < 0.16$. In the percolative metallic phase, the volume fractions v_M of the metal and v_I of the insulator satisfy $v_M + v_I = 1$ and $0.16\, v_M = n_f$ (Maxwell construction in a two-phase state). At the percolation threshold $v_M \sim 0.62$, which is close to the critical occupation for the square lattice site percolation problem. The very low value of the resistivity of the 10 u.c. samples suggests a proximity to the homogeneous phase and a sizable carrier concentration, so we estimate $n_f = 0.14$, i.e., $v_M = 88\%$.

In the effective Hamiltonian $\mathcal{H}_{\text{eff}}$ [Eq. (2) of the main text], the anisotropy tensor A has nonzero elements in the plane of the interface. Due to the tilt and rotation of the TiO$_6$ octahedra in LTO, hopping amplitudes are given by a nondiagonal matrix [54] such that the interfacial DM mostly affects ϕ.

To see the stability of the spiral state, we checked that the demagnetizing energy due to the small ferromagnetic component at the boundaries [55] does not alter the spiral magnetic ground state. The stability of the spiral, when a magnetic field is applied perpendicularly to the interface, depends on the strength of the in-plane DM of LTO and of the exchange asymmetry. Using values listed in Ref. [54], with a typical

anisotropy parameter $A \simeq 2$ meV, we estimate that moments align along z when the magnetic field B exceeds $\sim$20T, which is above the maximum field available in our magnetotransport measurements.

2. Mobility in the spin spiral domains

As can be seen in Fig. 3 of the main text, the linear scale of the magnetic modulation region is on the order of a micrometer. According to the scenario that we advocated to explain its origin, this suggests that the spin diffusion length, λ_s, has a similar magnitude. As electrons move through the stripe pattern, they experience spin scattering due to the change in the direction of alignment of the local moments, perpendicularly to the stripe. Following Ref. [70], we determine the transmission T and reflection R coefficients *a la* Landauer-Büttiker, for electrons traveling across a structure consisting of two antiferromagnetically ordered regions separated by a paramagnetic spacer layer. The direction of the alignment in the second region is at an angle θ with respect to that in the first region. The system is equivalent to a Fabry-Pérot interferometer, so that we model one period of the spin spiral pattern as $d/\mathbf{a_0}$ interferometers in series ($d = 160$ nm, $\mathbf{a_0} = 4$ Å). A priori one should include two main types of processes. In the direct process, a portion T of the wave hits interferometer n and is subsequently transmitted to $n + 1$. In the indirect process, the portion R of the wave that is reflected from interferometer n, travels in the backward direction toward interferometer m, where part of it is reflected and then moves in the forward direction toward interferometer n where it adds its contribution to the transmitted portion T of the initial wave; the amplitude of this indirect process is at most $T^{n-m}R^2$, which decreases exponentially with $(n - m)$; in addition it contains a phase factor, which stems from the $2(n - m)a_0$ distance involved in the indirect process, producing a phase difference between the two amplitudes. Overall, we neglect these secondary processes, which introduce small corrections to T and R. For $\theta = \frac{2\pi}{d}\mathbf{a_0} \sim 0.016$, $T \sim 0.999$ [70] and over a distance $\lambda_s \sim 1$ μm, there are $\frac{\lambda_s}{\mathbf{a_0}}$ interferometers. The ratio of the mobility in the presence of the spin spiral over the mobility in its absence is $T^{\lambda_s/\mathbf{a_0}}/(1 - T^{\lambda_s/\mathbf{a_0}}) \sim 0.05$. Consequently, the mobility in the stripe region is at least one order of magnitude smaller than in the rest of the sample.

---

[1] A. A. Abrikosov, Phys. Rev. B **58**, 2788 (1998).

[2] D. D. Majumder and S. Karan, in *Ceramic Nanocomposites* (Elsevier, Amsterdam, 2013), pp. 51–91.

[3] S. Jin, T. H. Tiefel, M. McCormack, R. A. Fastnacht, R. Ramesh, and L. H. Chen, Science **264**, 413 (1994).

[4] C. Lin, C. Yi, Y. Shi, L. Zhang, G. Zhang, J. Müller, and Y. Li, Phys. Rev. B **94**, 224404 (2016).

[5] P. Sinjukow and W. Nolting, Phys. Rev. B **68**, 125107 (2003).

[6] S. Jin, M. McCormack, T. H. Tiefel, and R. Ramesh, J. Appl. Phys. **76**, 6929 (1994).

[7] M. A. Subramanian, B. H. Toby, A. P. Ramirez, W. J. Marshall, A. W. Sleight, and G. H. Kwei, Science **273**, 81 (1996).

[8] H. Röder, J. Zang, and A. R. Bishop, Phys. Rev. Lett. **76**, 1356 (1996).

[9] N. Maksimovic, I. M. Hayes, V. Nagarajan, J. G. Analytis, A. E. Koshelev, J. Singleton, Y. Lee, and T. Schenkel, Phys. Rev. X **10**, 041062 (2020).

[10] M. A. McGuire, Q. Zhang, H. Miao, W. Luo, M. Yoon, Y. Liu, T. Yilmaz, and E. Vescovo, Chem. Mater. **33**, 9741 (2021).

[11] F. Wei, X. P. A. Gao, S. Ma, and Z. Zhang, Phys. Status Solidi (b) **256**, 1900139 (2019).

[12] C. M. Wang and X. L. Lei, Phys. Rev. B **86**, 035442 (2012).

[13] W. Zhang, R. Yu, W. Feng, Y. Yao, H. Weng, X. Dai, and Z. Fang, Phys. Rev. Lett. **106**, 156808 (2011).

[14] D. Shoenberg, *Magnetic Oscillations in Metals* (Cambridge University Press, Cambridge, UK, 1984).

[15] S. Datta, *Electronic Transport in Mesoscopic Systems* (Cambridge University Press, Cambridge, UK, 1997).

[16] M. M. Parish and P. B. Littlewood, Nature (London) **426**, 162 (2003).

[17] M. M. Parish and P. B. Littlewood, Phys. Rev. B **72**, 094417 (2005).

[18] N. V. Kozlova, N. Mori, O. Makarovsky, L. Eaves, Q. D. Zhuang, A. Krier, and A. Patanè, Nat. Commun. **3**, 1097 (2012).

[19] S. Mallik, G. C. Ménard, G. Saïz, I. Gilmutdinov, D. Vignolles, C. Proust, A. Gloter, N. Bergeal, M. Gabay, and M. Bibes, Nano Lett. **22**, 65 (2022).

[20] J. C. W. Song, G. Refael, and P. A. Lee, Phys. Rev. B **92**, 180204(R) (2015).

[21] J. Meng, X. Chen, M. Liu, W. Jiang, Z. Zhang, J. Ling, T. Shao, C. Yao, L. He, R. Dou, C. Xiong, and J. Nie, J. Phys.: Condens. Matter **32**, 355703 (2020).

[22] X. Yang, H. Bai, Z. Wang, Y. Li, Q. Chen, J. Chen, Y. Li, C. Feng, Y. Zheng, and Z. Xu, Appl. Phys. Lett. **108**, 252401 (2016).

[23] R. Xu, A. Husmann, T. F. Rosenbaum, M. L. Saboungi, J. E. Enderby, and P. B. Littlewood, Nature (London) **390**, 57 (1997).

[24] A. Husmann, J. B. Betts, G. S. Boebinger, A. Migliori, T. F. Rosenbaum, and M. L. Saboungi, Nature (London) **417**, 421 (2002).

[25] M. Lee, T. F. Rosenbaum, M.-L. Saboungi, and H. S. Schnyders, Phys. Rev. Lett. **88**, 066602 (2002).

[26] M. Novak, S. Sasaki, K. Segawa, and Y. Ando, Phys. Rev. B **91**, 041203(R) (2015).

[27] X. Huang, L. Zhao, Y. Long, P. Wang, D. Chen, Z. Yang, H. Liang, M. Xue, H. Weng, Z. Fang, X. Dai, and G. Chen, Phys. Rev. X **5**, 031023 (2015).

[28] J. Xiong, S. Kushwaha, J. Krizan, T. Liang, R. J. Cava, and N. P. Ong, Europhys. Lett. **114**, 27002 (2016).

[29] A. Narayanan, M. D. Watson, S. F. Blake, N. Bruyant, L. Drigo, Y. L. Chen, D. Prabhakaran, B. Yan, C. Felser, T. Kong, P. C. Canfield, and A. I. Coldea, Phys. Rev. Lett. **114**, 117201 (2015).

[30] J. Feng, Y. Pang, D. Wu, Z. Wang, H. Weng, J. Li, X. Dai, Z. Fang, Y. Shi, and L. Lu, Phys. Rev. B **92**, 081306(R) (2015).

[31] J. Zhang, J. M. Ok, Y.-Y. Pai, J. Lapano, E. Skoropata, A. R. Mazza, H. Li, A. Huon, S. Yoon, B. Lawrie, M. Brahlek, T. Z. Ward, G. Eres, H. Miao, and H. N. Lee, Phys. Rev. B **104**, L161404 (2021).

[32] A. A. Abrikosov, Europhys. Lett. **49**, 789 (2000).

[33] A. L. Friedman, J. L. Tedesco, P. M. Campbell, J. C. Culbertson, E. Aifer, F. K. Perkins, R. L. Myers-Ward, J. K. Hite, C. R. Eddy, G. G. Jernigan, and D. K. Gaskill, Nano Lett. **10**, 3962 (2010).

[34] J. Y. Chen, J. F. Feng, and J. M. D. Coey, Appl. Phys. Lett. **100**, 142407 (2012).

[35] R. U. R. Sagar, M. Galluzzi, C. Wan, K. Shehzad, S. T. Navale, T. Anwar, R. S. Mane, H.-G. Piao, A. Ali, and F. J. Stadler, ACS Appl. Mater. Interfaces **9**, 1891 (2017).

[36] Y. He, J. Gayles, M. Yao, T. Helm, T. Reimann, V. Strocov, W. Schnelle, M. Nicklas, Y. Sun, G. H. Fecher, and C. Felser, Nat. Commun. **12**, 4576 (2021).

[37] W. Niu, Y. Gan, Z. Wu, X. Zhang, Y. Wang, Y. Chen, L. Wang, Y. Xu, L. He, Y. Pu, and X. Wang, Adv. Mater. Interfaces **8**, 2101235 (2021).

[38] Z.-C. Wang, L. Chen, S.-S. Li, J.-S. Ying, F. Tang, G.-Y. Gao, Y. Fang, W. Zhao, D. Cortie, X. Wang, and R.-K. Zheng, npj Quantum Mater. **6**, 53 (2021).

[39] C. W. Schneider, S. Thiel, G. Hammerl, C. Richter, and J. Mannhart, Appl. Phys. Lett. **89**, 122101 (2006).

[40] J. Biscaras, N. Bergeal, A. Kushwaha, T. Wolf, A. Rastogi, R. Budhani, and J. Lesueur, Nat. Commun. **1**, 89 (2010).

[41] A. P. Ramirez, J. Phys.: Condens. Matter **9**, 8171 (1997).

[42] M. J. Veit, R. Arras, B. J. Ramshaw, R. Pentcheva, and Y. Suzuki, Nat. Commun. **9**, 1458 (2018).

[43] J. Dufouleur, L. Veyrat, B. Dassonneville, C. Nowka, S. Hampel, P. Leksin, B. Eichler, O. G. Schmidt, B. Büchner, and R. Giraud, Nano Lett. **16**, 6733 (2016).

[44] A. T. Lonchakov and S. B. Bobin, Appl. Phys. Lett. **118**, 062106 (2021).

[45] H. Jin, K. Lee, S. H. Baek, J. S. Kim, B. K. Cheong, B. H. Park, S. Yoon, B. J. Suh, C. Kim, S. S. Seo, and S. Lee, Sci. Rep. **6**, 34295 (2016).

[46] K. J. Kormondy, L. Gao, X. Li, S. Lu, A. B. Posadas, S. Shen, M. Tsoi, M. R. McCartney, D. J. Smith, J. Zhou, L. L. Lev, M. A. Husanu, V. N. Strocov, and A. A. Demkov, Sci Rep. **8**, 7721 (2018).

[47] A. Patanè, W. H. M. Feu, O. Makarovsky, O. Drachenko, L. Eaves, A. Krier, Q. D. Zhuang, M. Helm, M. Goiran, and G. Hill, Phys. Rev. B **80**, 115207 (2009).

[48] J. Hu, M. M. Parish, and T. F. Rosenbaum, Phys. Rev. B **75**, 214203 (2007).

[49] W. J. Wang, K. H. Gao, Z. Q. Li, T. Lin, J. Li, C. Yu, and Z. H. Feng, Appl. Phys. Lett. **105**, 182102 (2014).

[50] F. Börrnert, F. Kern, F. Harder, T. Riedel, H. Mueller, B. Büchner, and A. Lubk, Ultramicroscopy **203**, 12 (2019).

[51] D. V. Christensen, Y. Frenkel, Y. Z. Chen, Y. W. Xie, Z. Y. Chen, Y. Hikita, A. Smith, L. Klein, H. Y. Hwang, N. Pryds, and B. Kalisky, Nat. Phys. **15**, 269 (2019).

[52] B. Kalisky, E. M. Spanton, H. Noad, J. R. Kirtley, K. C. Nowack, C. Bell, H. K. Sato, M. Hosoda, Y. Xie, Y. Hikita, G. Woltmann, C. and Pfanzelt, R. Jany, C. Richter, H. Y. Hwang, J. Mannhart, and K. A. Moler, Nat. Mater. **12**, 1091 (2013).

[53] G. I. Meijer, W. Henggeler, J. Brown, O.-S. Becker, J. G. Bednorz, C. Rossel, and P. Wachter, Phys. Rev. B **59**, 11832 (1999).

[54] R. Schmitz, O. Entin-Wohlman, A. Aharony, A. B. Harris, and E. Müller-Hartmann, Phys. Rev. B **71**, 144412 (2005).

[55] M. Gabay and T. Garel, J. Physique **46**, 5 (1985).

[56] S. Banerjee, O. Erten, and M. Randeria, Nat. Phys. **9**, 626 (2013).

[57] M. Gabay and J.-M. Triscone, Nat. Phys. **9**, 610 (2013).

[58] H. Ishida and A. Liebsch, Phys. Rev. B **77**, 115350 (2008).

[59] J. Biscaras, Thesis, Chapter 5, Université Pierre et Marie Curie-Paris VI (2012).

[60] A. David, Y. Tian, P. Yang, X. Gao, W. Lin, A. B. Shah, J. M. Zuo, W. Prellier, and T. Wu, Sci. Rep. **5**, 10255 (2015).

[61] J. M. Ok, N. Mohanta, J. Zhang, S. Yoon, S. Okamoto, E. S. Choi, H. Zhou, M. Briggeman, P. Irvin, A. R. Lupini, Y. Y. Pai, E. Skoropata, C. Sohn, H. Li, H. Miao, B. Lawrie, W. S. Choi, G. Eres, J. Levy, and H. N. Lee, Sci. Adv. **7**, eabf9631 (2021).

[62] P. Scheiderer, M. Schmitt, J. Gabel, M. Zapf, M. Stübinger, P. Schütz, L. Dudy, C. Schlueter, T.-L. Lee, M. Sing, and R. Claessen, Adv. Mater. **30**, 1706708 (2018).

[63] S. Tanuma, C. J. Powell, and D. R. Penn, Surf. Interface Anal. **35**, 268 (2003).

[64] E. H. Sondheimer, Phys. Rev. **80**, 401 (1950).

[65] W. A. Harrison, Phys. Rev. **118**, 1190 (1960).

[66] M. R. van Delft, Y. Wang, C. Putzke, J. Oswald, G. Varnavides, C. A. C. Garcia, C. Guo, H. Schmid, V. Süss, H. Borrmann, J. Diaz, Y. Sun, C. Felser, B. Gotsmann, P. Narang, and P. J. W. Moll, Nat. Commun. **12**, 4799 (2021).

[67] A. Lubk, Holography and tomography with electrons, in *Advances in Imaging and Electron Physics* Vol. 206 (Academic Press, San Diego, CA, 2018).

[68] J. M. Kurdestany and S. Satpathy, Phys. Rev. B **96**, 085132 (2017).

[69] N. Nakagawa, H. Y. Hwang, and D. A. Muller, Nat. Mater. **5**, 204 (2006).

[70] A. S. Núñez, R. A. Duine, P. Haney, and A. H. MacDonald, Phys. Rev. B **73**, 214426 (2006).